processes

MDPI

Article

Heterogeneous Photocatalytic Degradation of a Glucocorticoid in Aqueous Solution and Industrial Wastewater Using TiO_2-Zn(II)-Clinoptilolite Catalyst

Andrea G. Briseño-Peña [1], Monserrat Castañeda-Juárez [1], Verónica Martínez-Miranda [1], Ivonne Linares-Hernández [1,*], Fortunata Santoyo-Tepole [2], Marcos Solache-Ríos [3], Elia Alejandra Teutli-Sequeira [1,4], Carlos R. Fonseca [1] and Mario Esparza-Soto [1]

1 Instituto Interamericano de Tecnología y Ciencias del Agua (IITCA), Universidad Autónoma del Estado de México, Unidad San Cayetano, Km. 14.5, Carretera, Toluca-Atlacomulco, Toluca C.P. 50200, Mexico; agbrisenop001@alumno.uaemex.mx (A.G.B.-P.); mcastanedaj_s@uaemex.mx (M.C.-J.); mmirandav@uaemex.mx (V.M.-M.); eateutlis@uaemex.mx (E.A.T.-S.); crfonsecao@uaemex.mx (C.R.F.); mesparzas@uaemex.mx (M.E.-S.)
2 Escuela Nacional de Ciencias Biológicas, Instituto Politécnico Nacional, Prolongación de Carpio y Plan de Ayala, Col. Santo Tomás, Miguel Hidalgo C.P. 11340, Mexico; tepole@hotmail.com
3 Departamento de Química, Instituto Nacional de Investigaciones Nucleares, Carretera México-Toluca S/N, La Marquesa, Ocoyoacac C.P. 52750, Mexico; mjsolacher_ext@uaemex.mx
4 Secretaria de Ciencias, Humanidades, Tecnología e Innovación SECIHTI, Cátedras SECIHTI, Ciudad de México C.P. 03940, Mexico
* Correspondence: ilinaresh@uaemex.mx

Abstract

Dexamethasone (DXM) is a glucocorticoid widely used in treating various diseases, but its extensive use raises environmental concerns due to poor absorption and rapid excretion, leading to its presence in aquatic environments. In this study, aqueous DXM was treated via heterogeneous solar photocatalysis (HSP) using a Zn-doped TiO_2 catalyst supported on zeolite clinoptilolite (TiO_2-Zn(II)-ZC), synthesized by electrodeposition. The catalyst was characterized by IR spectroscopy, SEM-EDS, XRD, atomic absorption spectroscopy, and P_{zc} determination. A Box–Behnken design was applied to evaluate the influence of initial DXM concentration (5–15 mg/L), hydraulic retention time (HRT: 30–60 min), and catalyst dose (0.5–1.5 g/L), using DXM (UV–Vis) and COD as response variables. Optimal conditions (12.5 mg/L DXM, 60 min HRT, 1.0 g/L catalyst) achieved 80% DXM removal (UV–Vis), 88.71% (HPLC), 85.29% COD removal, and 82.86% TOC reduction at 67 °C, 325.12 kJ/L, and 38.77 W/m^2. Additionally, a treated sample of chocolate industry wastewater enriched with 12.5 mg/L DXM (DXM-WW) achieved 67.88% (HPLC), 93.02% (COD), and 92.38% (TOC) removal. The catalyst reduced the bandgap, enabling sunlight-driven generation of e^-/h^+ pairs and reactive oxygen species ($^{\bullet}OH$, H_2O_2, and $O_2^{\bullet-}$), facilitating DXM degradation.

Keywords: pharmaceutical drugs; zeolite; advanced oxidation processes; solar radiation; electrodeposition

check for updates

Academic Editor: Christos Argirusis

Received: 6 August 2025
Revised: 25 August 2025
Accepted: 26 August 2025
Published: 29 August 2025

Citation: Briseño-Peña, A.G.; Castañeda-Juárez, M.; Martínez-Miranda, V.; Linares-Hernández, I.; Santoyo-Tepole, F.; Solache-Ríos, M.; Teutli-Sequeira, E.A.; Fonseca, C.R.; Esparza-Soto, M. Heterogeneous Photocatalytic Degradation of a Glucocorticoid in Aqueous Solution and Industrial Wastewater Using TiO_2-Zn(II)-Clinoptilolite Catalyst. *Processes* **2025**, *13*, 2781. https://doi.org/10.3390/pr13092781

Copyright: © 2025 by the authors. Licensee MDPI, Basel, Switzerland. This article is an open access article distributed under the terms and conditions of the Creative Commons Attribution (CC BY) license (https://creativecommons.org/licenses/by/4.0/).

1. Introduction

Corticosteroids are essential stress hormones, either produced endogenously or administered as pharmaceuticals or veterinary agents. They are typically classified as glucocorticoids or mineralocorticoids and are widely used to treat various medical conditions, primarily as anti-inflammatory agents [1–3]. Dexamethasone (DXM), a synthetic glucocorticoid, structurally similar to the endogenous hormone cortisol, exhibits enhanced

anti-inflammatory potency, approximately 25 times greater, due to key structural modifications, including a fluorine atom at position C9, unsaturation between C1 and C2 forming a cross-conjugated dienone system, and a methyl group at C16 (Figure 1) [4–7].

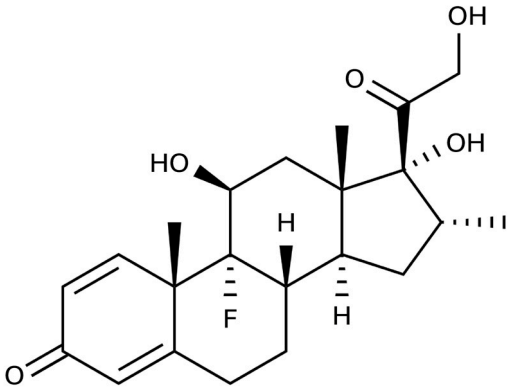


Figure 1. DXM ($C_{22}H_{29}FO_5$) structure.

DXM has been frequently detected in surface water, with reported concentrations up to 8.78 ng/L. In drinking water, maximum concentrations of 0.37 ng/L and 2.11 ng/L have been observed. Arvaniti et al. [2] reported that DXM concentrations can reach as high as 1050.90 ng/L in wastewater, 2.11 ng/L in river water, and 8.78 ng/L in tap water. Although these concentrations are generally low (in the μg/L to ng/L range), the presence of DXM in aquatic environments is a growing concern due to its potential chronic toxicity. Even at trace levels, glucocorticoids such as DXM can disrupt aquatic ecosystem, affecting the reproduction, growth, and development of fish and other organisms [8].

Advanced oxidation processes (AOPs) have emerged as effective technologies for degrading different pollutants. These processes generate highly reactive oxidizing species, primarily hydroxyl radicals ($^{\bullet}$OH), which possess a high oxidation potential (2.8 V) and can non-selectively oxidize a wide range of organic contaminants [9,10]. Various AOPs have been successfully applied for the degradation of DXM, electro-peroxone coupled with ultrasonic irradiation (78.7% TOC and 94.4% COD removal) [4], ozonation (95%) [8], sonochemical oxidation [7], thermally activated persulfate at pH 7 (100%) [2], and pulsed corona discharge with the addition of peroxydisulfate, peroxymonosulfate, and hydrogen peroxide [3] Other effective treatments include UV/persulphate (100%) [11], anodic oxidation [12], UV/$S_2O_8^{2-}$/Al_2O_3 (94%) [13], and direct photolysis (100%) [14].

Photocatalysis involves the use of semiconductor catalysts such as TiO_2 and ZnO, which, under ultraviolet (UV) irradiation, absorb photons and promote the excitation of electrons from the valence band (VB) to the conduction band (CB). This excitation generates photo-induced electrons (e^-) in the CB and holes (h^+) in the VB, which subsequently participate in redox reactions that lead to the formation of reactive radicals, as shown in Equations (1)–(4). This process is initiated when the energy of the incident photon is equal to or greater than the bandgap energy of the semiconductor material [15]. The efficiency of the photocatalytic process is influenced by several operational parameters, including the type of radiation, catalyst and pollutant concentrations, water matrix composition, temperature, dissolved oxygen concentration, and pH [16].

$$h^+ + H_2O \rightarrow H^+ + HO^{\bullet} \quad (1)$$

$$h^+ + HO^- \rightarrow HO^{\bullet} \quad (2)$$

$$e^- + O_2 \rightarrow O_2^{\bullet} \quad (3)$$

$$e^- + O_2 + 2H_2O \rightarrow H_2O_2 + 2HO^\bullet \quad (4)$$

TiO_2 is a widely used photocatalyst due to its non-toxicity, stability, and high activity, but its wide bandgap (~3.2 eV) restricts absorption to the UV region and promotes e^-/h^+ recombination. Modification strategies such as transition metal doping introduce impurity levels that reduce the bandgap, extend visible-light absorption, and suppress charge recombination [17,18]. Traditionally, photocatalysts are used in suspension, which can complicate recovery and reuse. To address this, semiconductor materials can be immobilized onto solid supports such as glass beads, pebbles, sand, activated carbon, natural pumice, ceramics, and zeolites [19]. Among them, zeolites are especially attractive owing to their high surface area, adsorption capacity, and ability to reduce e^-/h^+ recombination, which enhances photocatalytic efficiency [19–21].

As previously reported, the goal of this research lies in the synthesis of a modified TiO_2-Zn(II)-clinoptilolite catalyst via the electrodeposition method and its application in HSP. The catalyst electrosynthesis consisted of using Zn anode/cathode, with an effective surface area of 17 cm^2, at 0.5 A, 2 h, 200 g of zeolite clinoptilolite (ZC), 1 L of distilled water, 2 g of NaCl as support electrolyte, pH 7.1 and at room temperature. In total, 2.2 mg Zn/g TiO_2-Zn(II)-ZC was obtained; this modification reduces the TiO_2 bandgap and enhances the generation of e^-/h^+ pairs through solar photoactivation. The photocatalyst system employed a channel parabolic concentrator (CPC) reactor, enabling efficient utilization of solar energy. The heterogeneous photocatalytic degradation of DXM was investigated: the operational parameters were the initial concentration of DXM in aqueous solution, hydraulic retention time (HRT), and ratio catalyst mass/solution volume (M/V). The main response variables were DXM concentration and chemical oxygen demand (COD). Additionally, the treatment system was evaluated using real wastewater from the chocolate industry. The main contribution of this work is the electrosynthesis of the catalyst. Electrodeposition is an in situ dissolution method that can be carried out at room temperature, natural pH, and in the absence of intermediate phases that impurify the products, obtaining small crystals with a large surface area. Another advantage is the direct and uniform deposition of metal of high purity. The sol-gel, the co-precipitation, and the solid-phase reaction methods are among the primary techniques used for synthesizing Zn-doped TiO_2, enhancing photocatalytic activity, particularly in the visible light region. In general terms, these methods present specific operating conditions; for example, the use of precursors, high temperatures (300–1000 °C), acid pH, complexity in reagent handling, and longer synthesis times.

2. Materials and Methods

2.1. Methods

A commercial injectable solution of dexamethasone phosphate (Metax® SON'S Laboratory, Atlixcayotl, Puebla, Mexico, 8 mg/2 mL) was used to prepare a standard solution at a concentration of 160 mg/L. The solution was analyzed using a UV–Vis spectrophotometer (Cary Varian 1E, Cary, NC, USA), software WinLab over a wavelength range of 200–800 nm to determine the maximum absorbance (λmax), which was observed at 243 nm. Calibration standards were prepared at concentrations of 4, 8, 12, 16, and 20 mg/L.

Samples of DXM solution and chocolate industry wastewater samples (DXM-WW) were characterized for various physicochemical parameters. COD was measured using the Hach method 8000 (range: 3–150 mg/L COD), and total organic carbon (TOC) was determined using the Hach Method 10173 (range: 20–150 mg/L C). Total phosphorus was analyzed using LCK348 (range: 0.5–5 mg/L P-PO_4^{3-}), and phosphate using the Hach method for the 1.5–15 mg/L PO_4^{3-} range. Nitrate and nitrite concentrations were determined using Hach methods 8039 (0.1–30 mg/L NO_3^--N) and 8507 (0.002–1.000 mg/L NO_2-N),

respectively. IR spectra were obtained using a Shimadzu Affinity-15 FTIR spectrometer 8 (Shimadzu Europe Duisburg, Duisburg, Germany) equipped with an ATR compartment for functional group identification, Software: Lab Solution IR.

High-performance liquid chromatography (HPLC) analysis was performed using an Agilent Technologies, (Santa Clara, CA, USA), 1260 Infinity LC system with a diode array detector (DAD). Chromatographic separation was achieved on a Zorbax SB C18 analytical column (5 µm, 150 mm × 4.6 mm) using an isocratic mobile phase of HPLC-grade water and acetonitrile at a flow rate of 1 mL/min. The column temperature was maintained at 30 °C, and DXM was detected at 275 nm.

2.2. Calibration Curve and Electrochemically Modification

Commercial zeolite clinoptilolite (ZC) was washed and dried at room temperature. Grains with sizes ranging from 0.5 to 2.5 cm were selected for catalyst preparation. The electrosynthesis of the catalyst was performed in a 2 L electrochemical batch cell. The cell contained 60 g of TiO_2 powder (Avantor Performance Materials) consisting of a mixed phase of anatase and rutile, 200 g of ZC, 1 L of distilled water, and 2 g of NaCl (Avantor Performance Materials) as supporting electrolyte. A monopolar electrochemical configuration was employed, using an array of Zn-Zn anode/cathode electrodes, each measuring 3.4 cm^3, with an effective surface area of 17 cm^2. The process was conducted at room temperature (pH 7.1) by applying a current of 0.5 A for 2 h. After synthesis, the material was thermally treated at 550 °C for 20 min using a Thermolyne Thermo Scientific—F6010 muflle furnace (Thermo Scientific, Waltham, MA, USA). The resulting catalyst was designated as TiO_2-Zn(II)-ZC.

Characterizations of both ZC and TiO_2-Zn(II)-ZC were performed by X-ray diffraction (XRD) using a Siemens D5000 diffractometer (Siemens, Munich, Germany) equipped with a copper-anode X-ray tube. Infrared (IR) spectroscopy and scanning electron microscopy (SEM) coupled with energy-dispersive X-ray spectroscopy (EDS) were carried out using a JEOL JSM-6610LV instrument (Oxford Instruments, Oxford, UK). The point of zero charge (P_{zc}) was determined according to the method reported by Castañeda-Juarez et al. [22]. The Zn content deposited on TiO_2-Zn(II)-ZC was determined by atomic absorption (AA) following acid digestion with a 2:1 mixture of HNO_3 and HCl using a CEM microwave digestion system (CEM Corporation, Matthews, NC, USA).

2.3. Heterogeneous Solar Photocatalysis Process (HSP)

The TiO_2-Zn(II)-ZC catalyst was packed in a borosilicate glass tube with 88% light transmittance and installed within a channel parabolic collector (CPC) reactor. The CPC was constructed using Alanod Miro-Sun® aluminum sheets (Ennepetal, Germany) shaped into a 60° parabolic profile, as shown in Figure 2. Photocatalytic trials were conducted between 11:30 a.m. and 2:30 p.m. to maximize solar irradiance. UV-A radiation was continuously monitored using a PMA2100 UV radiometer (Solar Light Company, Glenside, PA, USA). The sensor featured a spectral response range from 320 to 400 nm and a resolution of 0.001 mW/cm^2 to 200 mW/cm^2.

The accumulated energy (QUV) by the CPC was estimated using Equation (5):

$$QUV = QUVn - 1 + \Delta t_n \overline{UV}_{g,n} \frac{A_{CS}}{V_{ER}} \quad (5)$$

where n is the accumulated energy per unit volume (kJ/L), Δt_n is the time (s), A_{CS} is the area of solar radiation capture (m^2), V_{ER} is the volume (L), and $\overline{UV}_{g,n}$ is the incident solar irradiation (W/m^2) [23].

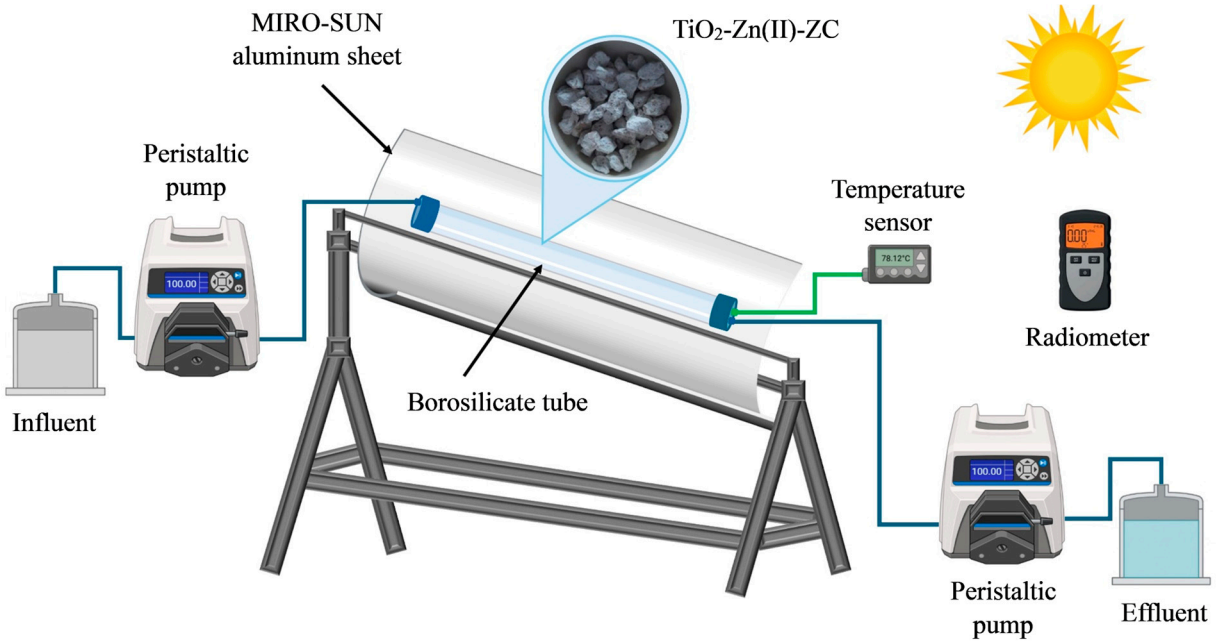


Figure 2. Reactor design for the HSP process.

2.3.1. Experimental Design

Response surface methodology, using a Box–Behnken design was employed to optimize the photocatalytic process, with statistical analysis performed using Statgraphics Centurion 19 software. Three independent variables were investigated at three levels each (Table 1): initial DXM concentration (5, 10, and 15 mg/L), hydraulic retention time (HRT: 30, 45, and 60 min), and catalyst M/V ratio of 0.5, 1.0, and 1.5 mg/L. The experimental matrix comprised 15 runs, including five degrees of freedom for error estimation (Table S1, Supplementary Materials). The response variables evaluated were DXM concentration, determined by UV–Vis spectrophotometry, and COD.

Table 1. Experimental levels and response variables.

Factor	Unidad	Level	Response (% Removal)
Initial concentration	mg/L	5, 10, 15	DXM by UV–Vis COD removal
Hydraulic retention time	min	30, 45, 60	
Catalyst mass/solution volume	mg/L	0.5, 1.0, 1.5	

To evaluate the contribution of individual components to the photocatalytic system, three control experiments were conducted: (a) Photolysis: a DXM solution (12.5 mg/L) was exposed to solar radiation for 60 min without the catalyst; (b) DXM at 12.5 mg/L, catalyst mass/solution volume (1.0 mg/L) in absence of UV light; and (c) Photocatalysis under artificial UV light: a DXM solution (12.5 mg/L) was treated with the catalyst (1.0 mg/L) under UV radiation provided by a GS-T5.003 lamp (5 W, λ = 380–400 nm, irradiance: 16 W/m^2).

2.3.2. Removal of DXM from Chocolate Industry Wastewater

A treated sample of chocolate industry wastewater was spiked with DXM at a concentration of 12.5 mg/L to evaluate the performance of the HSP process under real matrix conditions (the effluent was selected because of its high content of BOD, COD, and solids) to evaluate the interaction and behavior of DXM in the presence of organic matter. The sample was characterized according to the parameters described in Section 2.1. Photocat-

alytic treatment was subsequently carried out using the optimized operating conditions previously determined through response surface methodology with Statgraphics Centurion 19 software.

2.3.3. Kinetic Reaction

Kinetic experiments were performed under the optimal conditions for DXM degradation, as determined by the Box–Behnken design. Aliquots were collected at 5-minute intervals over a 60-minute period (5–60 min) and analyzed using UV–Vis spectrophotometry, HPLC, and COD measurements for both the aqueous solution and DXM-WW. For kinetic modeling, first-order, second-order, and the two-stage BMG models (Equations (6)–(8)) were applied. Model performance was evaluated based on the relationship between accumulated energy and DXM concentration. Kinetic constants were calculated using Statistica 10 StatSoft® software.

First-order kinetic model:

$$C_t = C_0 e^{-kt} \quad (6)$$

Second-order kinetic model:

$$C_t = \frac{C_0}{(C_0 kt + 1)} \quad (7)$$

BMG Model:

$$C_t = \left(\frac{t}{(m + bt)} - 1\right) C_0 \quad (8)$$

where C_0 is the initial concentration, C_t is the concentration at reaction time t, and m and b are the constants of the BMG model.

3. Results

3.1. Electrosynthesis of Zeolite and Characterization

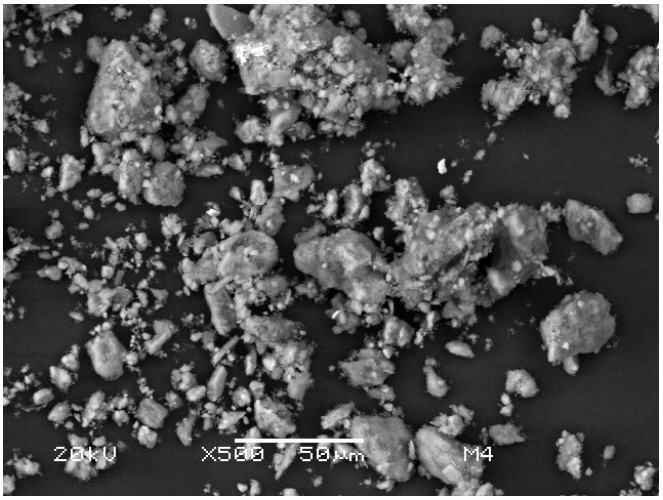
Figure 3 presents the SEM micrographs of the raw ZC and the synthesized TiO_2-Zn(II)-ZC catalyst. Figure 3a shows the surface morphology of ZC. In Figure 3b, the zeolite particles are visibly coated with TiO_2, indicating successful deposition. The synthesis method does not appear to alter the structural integrity of zeolite, which primarily functions as a support material. Figure 3c reveals TiO_2 agglomerates on the zeolite surface, and Figure 3d displays distinct bright spots attributed to the presence of zinc, indicating successful Zn incorporation into the TiO_2 structure supported on the ZC.

According to the EDS analysis summarized in Table 2, the major elements identified in TiO_2-Zn(II)-ZC initial are oxygen (50.80%), silicon (6.63%), titanium (35.7%), and zinc (3.66%), the value of oxygen is significantly higher in TiO_2-Zn(II)-ZC than in ZC, which could be due to oxidation of the surface of the crystals while removing the flux with water [24]. Other elements present in smaller proportions include aluminum, potassium, iron, and calcium. Figure S1 (Supplementary Materials) shows EDS spectra.

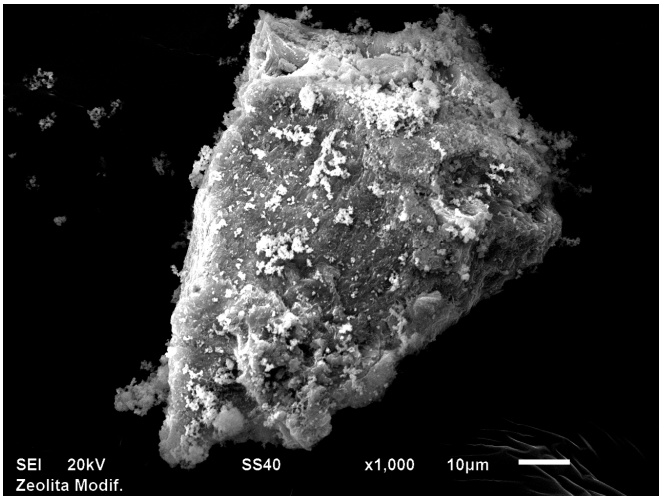
Zinc concentration was determined by AA for the following samples: (a) natural ZC (0.0066 mg Zn/g ZC), (b) Zn on TiO_2 (0.0126 mg Zn/g TiO_2), and (c) TiO_2-Zn(II)-ZC (2.2 mg Zn/g). These results confirmed that the combined electrosynthesis and thermal treatment was effective in immobilizing Zn on the ZC support. The calcination temperature (550 °C) enhanced photocatalytic activity, and the electrodeposition method helped prevent the presence of organic residues on the catalyst surface [25].

Table 2. Elemental composition of the modified material.

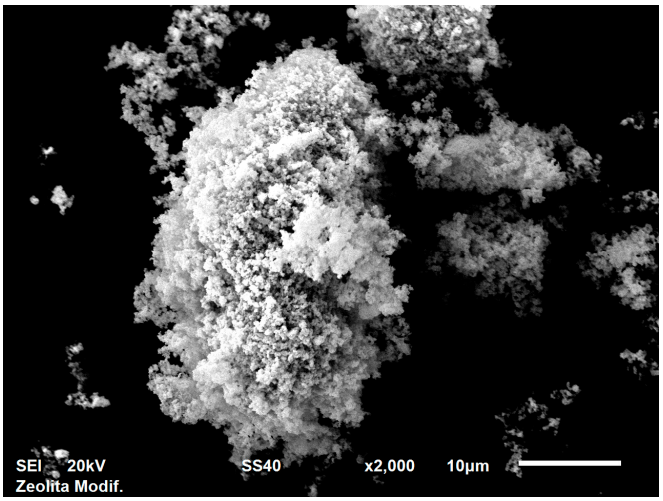
Elemental Composition (%)					
Element	**ZC**	**TiO_2-Zn(II)-ZC**			
		Initial	**Final**		
			0.5	**1.0**	**1.5**
O	41.89 ± 1.64	50.80 ± 1.06	36.41 ± 1.21	40.20 ± 2.14	39.41 ± 3.40
Al	4.81 ± 1.64	1.16 ± 0.75	6.57 ± 0.36	5.93 ± 0.70	6.88 ± 0.61
Si	26.69 ± 10.14	6.63 ± 4.42	39.24 ± 0.80	38.26 ± 4.38	36.28 ± 0.34
K	3.8 ± 1.80	1.10 ± 1.21	6.09 ± 0.69	5.64 ± 0.24	6.29 ± 2.33
Ca	9.02 ± 16.09	0.44 ± 0.21	2.26 ± 0.68	1.87 ± 0.55	2.36 ± 0.57
Ti	ND	35.7 ± 8.14	2.60 ± 0.79	4.93 ± 4.48	4.23 ± 1.22
Fe	1.5 ± 0.85	0.42 ± 0.49	2.71 ± 0.78	2.19 ± 0.50	3.67 ± 1.51
Zn	ND	3.66 ± 1.31	ND	ND	ND
Mg	0.62 ± 0.24	ND	0.80 ± 0.18	0.69 ± 0.09	0.84 ± 0.17
Na	ND	ND	ND	0.29 ± 0.49	ND



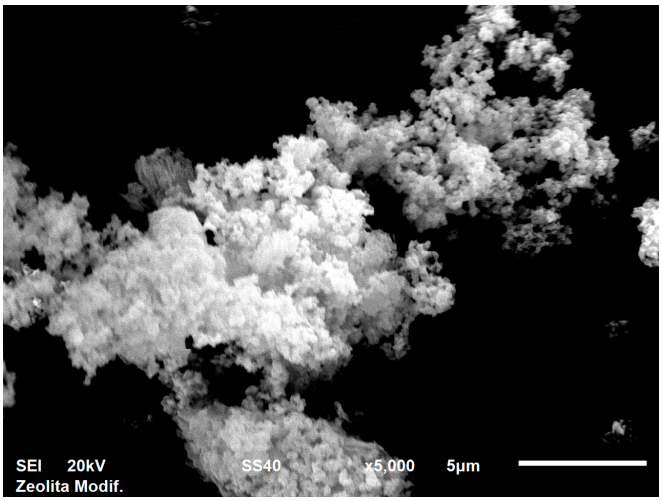
(**a**)



(**b**)



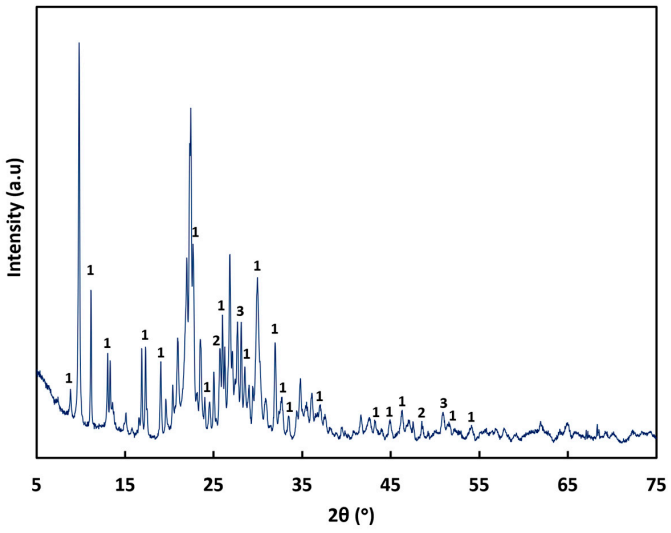
(**c**)



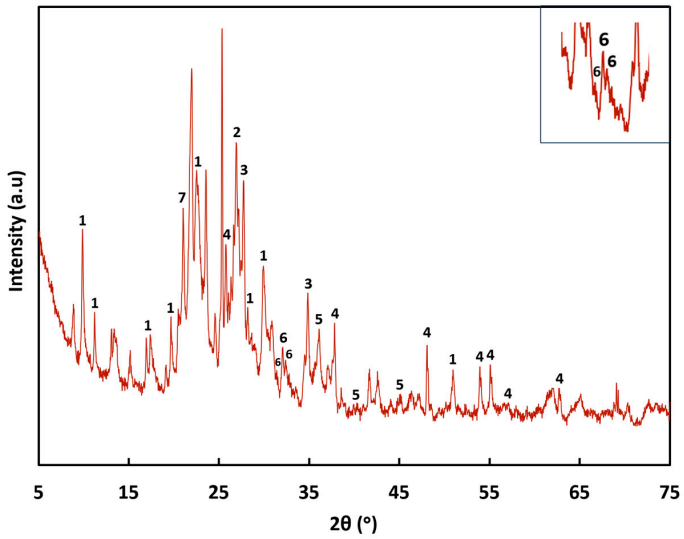
(**d**)

Figure 3. SEM analysis of ZC and TiO_2-Zn(II)-ZC: (**a**) ZC, (**b**) zeolite particles coated by TiO_2, (**c**) agglomerate of TiO_2 on the surface of the zeolite, and (**d**) bright spots associated with the presence of zinc fixed to TiO_2 and supported in the ZC.

Figure 4 shows XRD pattern of the (a) ZC, (b) TiO_2-Zn(II)-ZC, and (c) TiO_2-Zn(II)-ZC after DXM degradation. In the XRD pattern of the TiO_2-Zn(II)-ZC composite, diffraction peaks at 2θ = 25.78°, 37.78°, 48.05°, 53.88°, 55.11°, 57.16°, and 62.85° correspond to the anatase phase of TiO_2. Peaks at 2θ = 36.01°, 39.31°, and 45.21° are associated with the rutile phase. The anatase form is typically more photocatalytically active than rutile due to a higher density of localized states, increased surface-adsorbed •OH radicals, and a lower rate of e^-/h^+ recombination [25]. Additionally, peaks at 2θ = 31.50°, 32.05°, and 32.20° indicating the presence of the hexagonal crystalline structure of ZnO are identified [26]. The phase that contributes to catalytic activity is anatase. In the initial characterization of TiO_2-Zn(II)-ZC (Figure 4b), a mixture of anatase and rutile is observed where the peaks with the highest intensity correspond to anatase. Figure 4c shows the XRD of TiO_2-Zn(II)-ZC after DXM degradation, where only the anatase phase is identified while preserving its crystal structure, while the rutile phase loses crystallinity and the intensity of the peaks decreases considerably.

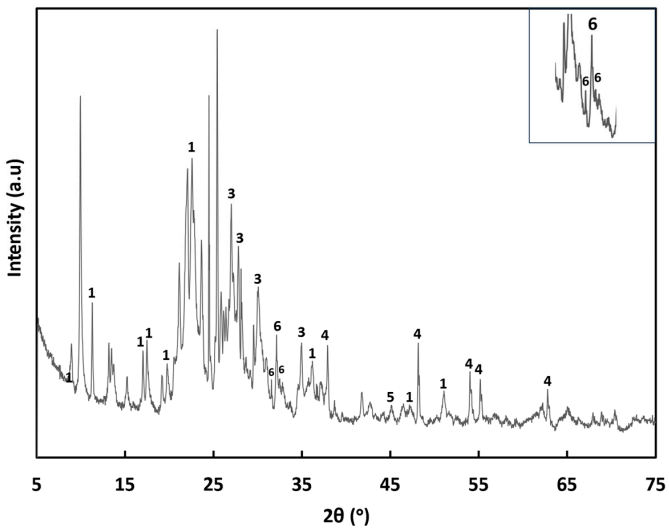


(**a**)



(**b**)

Figure 4. *Cont.*

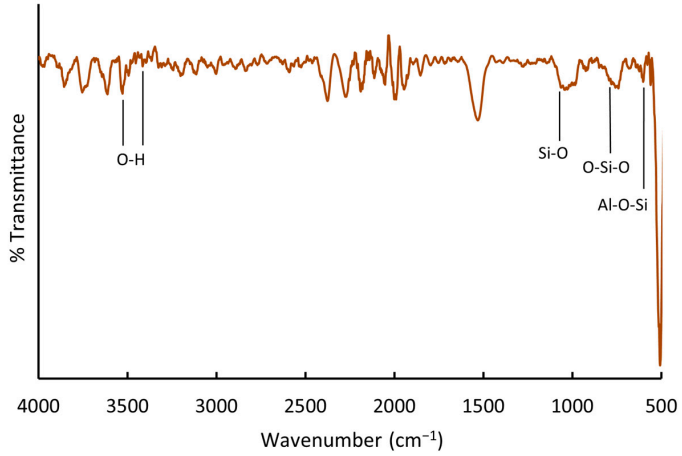


(**c**)

Figure 4. XRD pattern of the (**a**) ZC, (**b**) TiO_2-Zn(II)-ZC, and (**c**) TiO_2-Zn(II)-ZC after DXM degradation (1—clinoptilolite, 2—quartz, 3—albite, 4—TiO_2 anatase, 5—TiO_2 rutile, 6—ZnO (hexagonal), 7—silicon oxide.

According to the Joint Committee on Powder Diffraction Standards (JCPDS), the peaks observed in the XRD diffractograms correspond to silicon oxide (JCPDS 05-0490), quartz (JCPDS 47-1144), clinoptilolite (JCPDS 13-0304, 47-1870), albite (JCPDS 02-0515), and TiO_2 in the anatase phase (JCPDS 02-0387). Following the doping and support processes, characteristic peaks of TiO_2 and clinoptilolite remained visible in the diffractograms.

Figure 5 presents the IR spectra of the following: (a) ZC, (b) TiO_2, and (c) TiO_2-Zn(II)-ZC. In Figure 5a, a band at 599 cm^{-1} is observed, corresponding to torsional vibrations of Al−O−Si bonds in the zeolite structure. In Figure 5b, bands associated with the stretching vibrations of −OH groups and the scissor-like bending vibrations of water protons adsorbed on the TiO_2 surface are evident. Additionally, bands in the low-frequency region (500–633 cm^{-1}) are characteristic of Ti−O−Ti bonding. Figure 5c confirms the presence of Zn−O bonds, with absorption bands at 1033, 876, 749, and 521 cm^{-1}. These bands overlap with those associated with Ti−O−Ti, indicating successful Zn incorporation into the TiO_2 matrix. Table S2 (Supplementary Materials) summarizes the observed wavenumbers and their corresponding functional group assignments for ZC, TiO_2 y TiO_2-Zn(II)-ZC.



(**a**)

Figure 5. *Cont.*

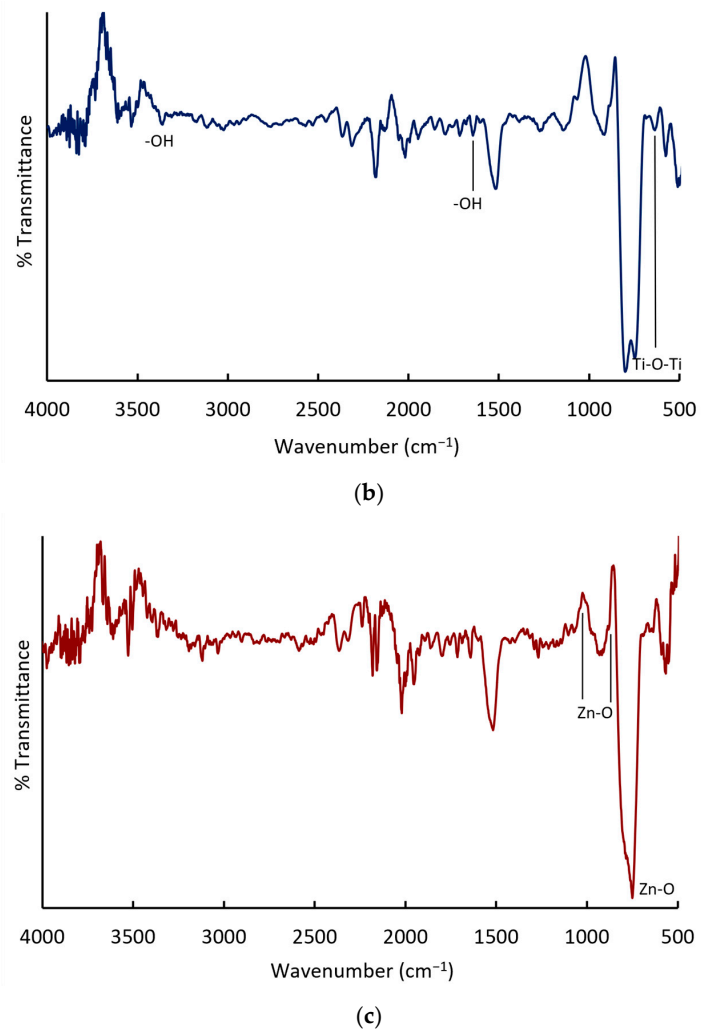


Figure 5. IR spectrum of (**a**) ZC, (**b**) TiO_2, (**c**) TiO_2-Zn(II)-ZC.

3.2. Characterization of DXM Aqueous Solution

DXM aqueous solutions were prepared at concentrations of 5, 10, and 15 mg/L for the experimental design. Corresponding COD values were determined at 38, 56, and 76 mg/L, respectively, showing a direct correlation between initial DXM concentration and COD. These COD values may also reflect the presence of excipients commonly added to pharmaceutical formulations alongside the active ingredient.

Figure 6 presents the IR spectrum of the injectable DXM solution. Key absorption bands include those at 1767 and 1667 cm^{-1}, corresponding to the stretching vibration of aliphatic ester and ketone carbonyl (C=O) groups. Broad bands at 3526 and 3377 cm^{-1} are attributed to the O−H stretching, while a strong C−F single bond is identified between 1100 and 1000 cm^{-1}, with characteristic overtones observed between 2600 and 2100 cm^{-1}. Additional bands at 2983 cm^{-1} are attributed to the C−H stretching vibrations. Peaks at 1710, 1162, and 1091 cm^{-1} correspond to C−O stretching vibrations of hydroxyl and ether groups [27]. The bands at 1568 and 1661 cm^{-1} are assigned to C=C bonds in cyclic compounds, while the band at 1092 cm^{-1} indicates the presence of C−OH groups. A distinctive band at 866 cm^{-1} corresponds to 1,4−diene−3−ketone bond vibrations. Finally, the band at 1100 cm^{-1} is characteristic of phosphate groups. Table S3 (Supplementary Materials) summarizes the observed wavenumbers and their associated functional groups in the DXM aqueous solution.

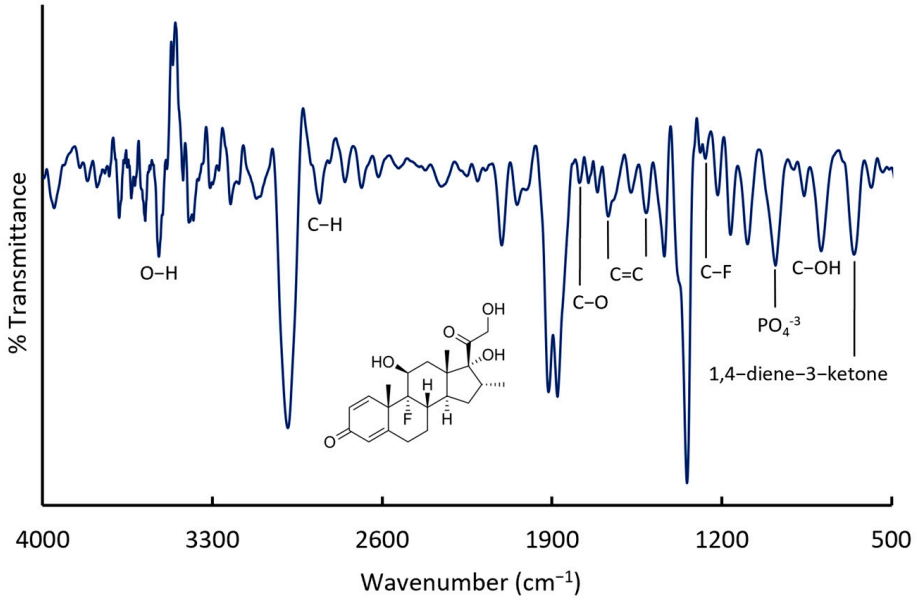


Figure 6. IR spectra of the DXM injectable solution.

3.3. Heterogeneous Solar Photocatalysis Process

HSP process was used to study the degradation of DXM, with optimal conditions determined through a Box–Behnken experimental design. The highest removal efficiencies, 70% for DXM and 63.16% for COD, were achieved in Experiment 6 (Table 3). This experiment was conducted with an initial DXM concentration of 5 mg/L, HRT of 30 min, and M/V ratio of 1.0 mg/L; the corresponding operational conditions included a temperature of 64.58 °C, accumulated energy 134.66 kJ/L, and incident radiation of 41.48 W/m^2 (Table 3).

Table 3. Obtained results from the experimental Box–Behnken design.

Experiment	Initial Concentration (mg/L)	HRT (min)	M/V (mg/L)	Removal (%)		T °C	Incident Radiation (W/m^2)	Accumulated Energy (kJ/L)
				DXM	COD			
1	5.0	45.0	1.5	50.00	34.21	62.78	41.17	210.05
2	10.0	30.0	1.5	66.00	46.43	62.23	43.92	158.62
3	10.0	60.0	1.5	65.00	41.07	44.37	30.08	195.32
4	5.0	60.0	1.0	54.00	42.11	65.11	47.02	304.48
5	15.0	45.0	1.5	60.00	43.42	63.63	37.17	184.98
6 *	5.0	30.0	1.0	70.00	63.16	64.58	41.48	134.66
7	15.0	60.0	1.0	63.33	55.26	74.76	41.31	140.03
8	5.0	45.0	0.5	38.00	18.42	66.32	36.20	188.23
9	10.0	30.0	0.5	58.00	44.64	62.20	40.70	145.69
10	10.0	45.0	1.0	65.00	48.21	42.98	41.89	154.89
11	10.0	60.0	0.5	58.00	44.64	45.91	40.19	220.32
12	15.0	45.0	0.5	53.33	46.05	58.83	50.89	168.44
13	10.0	45.0	1.0	64.00	42.86	73.07	44.01	198.67
14	15.0	30.0	1.0	44.00	22.37	37.75	43.01	132.89
15	10.0	45.0	1.0	67.00	47.32	72.70	42.05	220.00

* Experiment 6 exhibit the best removal efficiencies for Box–Behnken design.

In the HSP process, various factors influence removal efficiency. According to the ANOVA results (Table S4, Supplementary Materials), the most significant factors were the initial DXM concentration (p = 0.0436) and interaction between concentration and HRT (p = 0.0477). Other factors, including temperature, the presence or absence of UV light, and the M/V ratio, also affected the process but to a lesser extent. These key and secondary factors are discussed in detail below.

3.3.1. Concentration Initial Effect

According to the response surface plots, an increase in DXM concentration from 5 mg/L to 15 mg/L (at a constant M/V ratio of 1.0 mg/L) resulted in a decrease in removal efficiency from 70% to 44% (Figure 7a). A similar trend was observed for COD removal, which declined from 63.16% at lower concentrations to 22.37% at higher concentrations of DXM (Figure 7b). This reduction in efficiency is likely due to the saturation of active sites on the TiO_2-Zn(II)-ZC catalyst at higher pollutant concentrations, which hinders effective interaction between the catalyst and DXM molecules [28]. A comparable effect was reported by Pazoki et al. [29] who investigated the degradation of DXM (5–30 mg/L) using an Ag/TiO_2 photocatalyst (1500 mg/L) under UV irradiation (100–200 nm, 20 W) at pH 3 and 35 °C in a 600-mL batch reactor with an HRT of 240 min. The process achieved a removal efficiency of 77.6% for DXM.

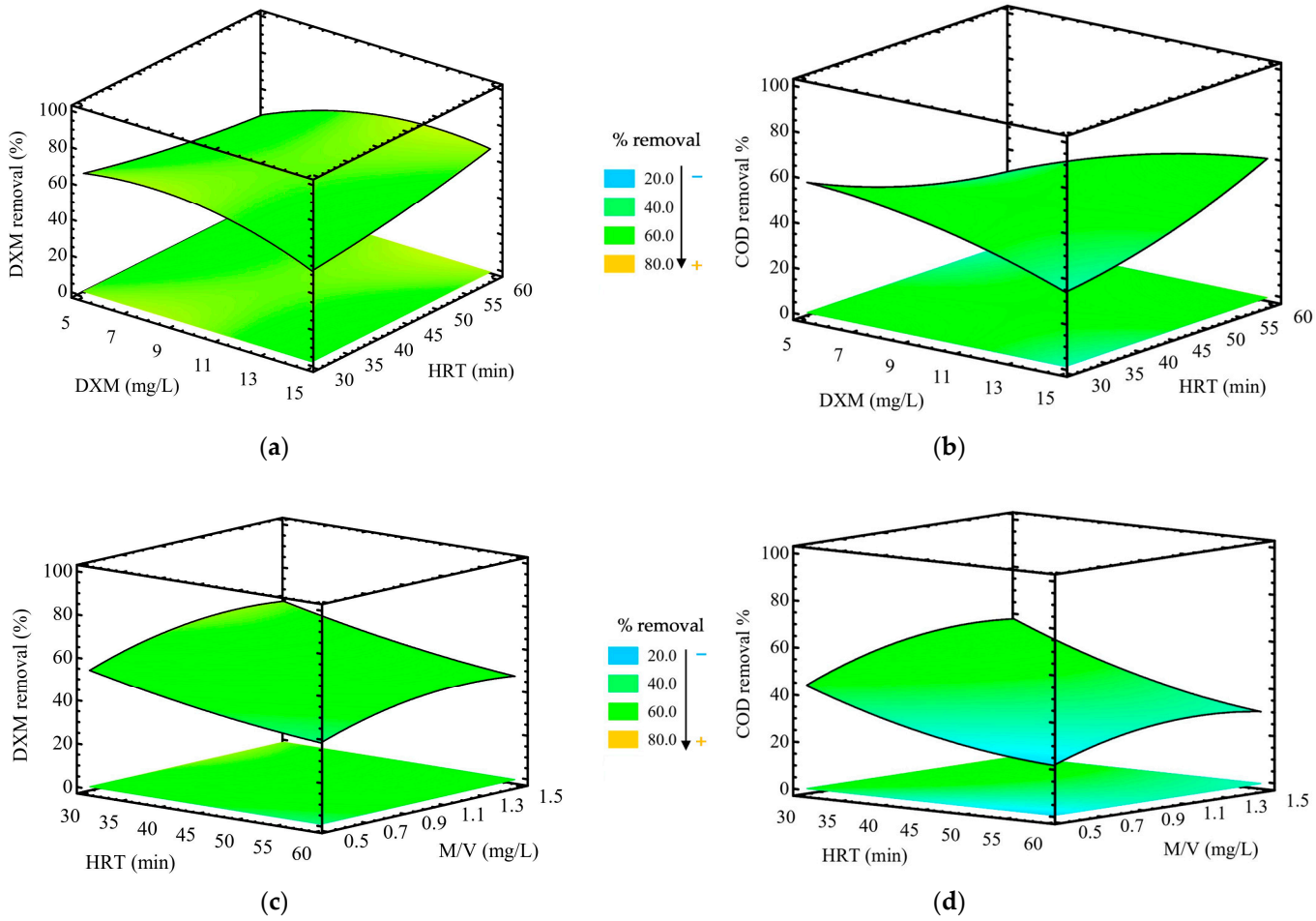
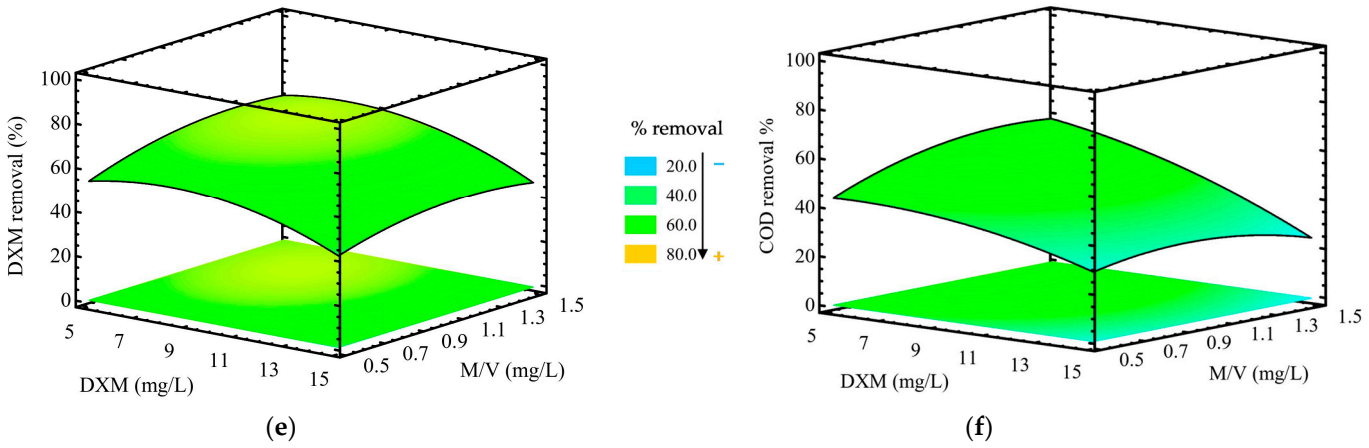


Figure 7. *Cont.*



(**e**) (**f**)

Figure 7. Response surface plots for the HSP process (**a**,**c**,**e**) show DXM removal percentages, while plots (**b**,**d**,**f**) show COD removal percentages under different experimental conditions.

Wilk et al. [30] evaluated the efficiency of heterogeneous photocatalysis under simulated sunlight for the degradation of DXM at a concentration of 1 mg/L using three photocatalysts: TiO_2 anatase, TiO_2 Degussa P25, and ZnO. Among them, TiO_2 Degussa P25 exhibited the highest photocatalytic activity, achieving 98.93% DXM degradation within 10 min. The experimental conditions included 100 mg/L of Degussa P25 TiO_2 at pH 7, simulated sunlight using a 150 W xenon lamp, continuous stirring, and a batch reactor setup.

3.3.2. Hydraulic Retention Time Effect

The removal efficiencies for DXM and COD increased with HRT, reaching a plateau at 60 min. However, based on the Box-Benhken experimental design, the highest removal rates, 70% for DXM and 63.16% for COD, were achieved within 30 min at an M/V ratio of 1.0 mg/L, an initial DXM concentration of 5 mg/L, and pH 5 (Figure 7c,d). A longer HRT allows for more effective contact between pollutants and the photocatalyst, enhancing the extent of photocatalytic degradation [31]. Ghenaatgar et al. [5] reported complete removal of 5 mg/L DXM after 140 min using 1500 mg/L ZrO_2 at pH 3. Pazoki et al. [29] achieved 77.6% removal of DXM (C_o = 5 mg/L) after 240 min with 1500 mg/L Ag-doped TiO_2 at pH 3 under a 20-W UV lamp.

3.3.3. Mass/Volume Ratio Effect

As shown in Figure 7e,f, the catalyst M/V ratio significantly affects the removal efficiencies of DXM and COD. At a low M/V ratio of 0.5 mg/L, removal efficiencies range from 38−58% for DXM and 18–40% for COD. Increasing the catalysts dosage increases the number of active sites available on the TiO_2-Zn(II)-ZC surface and promotes the generation of reactive species such as hydroxyl and superoxide radicals. However, exceeding the optimal catalyst concentration can lead to a decline in removal efficiency. Excess catalyst may scatter or block incident light, limiting photon absorption and reducing photocatalytic activity. Additionally, high catalyst concentrations may promote particle agglomeration, which decreases the effective surface area available for photon absorption and pollutant interaction, ultimately lowering the degradation rate [32,33].

3.3.4. Temperature Effect

Temperature plays a crucial role in determining the efficiency of photocatalytic processes. At the start of the experiments, ambient temperatures ranged from 17–23 °C. During the HSP, temperatures increased because of solar exposure, reaching 37.75–74.76 °C, depending on the climatic conditions. At 37.75 °C, the removal efficiencies were 44% for

DXM and 22.37% for COD. At the highest recorded temperature of 74.76 °C, efficiencies improved to 63.33% for DXM and 55.26% for COD. The highest removal rates, 70% for DXM and 63.16% for COD were observed in Experiment 6, conducted at 64.58 °C. These results indicate that photocatalytic performance improves with increasing temperature up to an optimal point. However, increasing the optimal temperature may lead to increased recombination of photogenerated e^-/h^+ pairs, thereby reducing the availability of these charge carriers for photocatalytic reactions.

While most photocatalytic processes are typically conducted near room temperature, the exothermic nature of pollutant degradation and recombination reactions can lead to a gradual rise in system temperature, further influencing the reaction kinetics and efficiency.

However, the rate of photodegradation tends to decrease after exceeding an optimal temperature. This decline is primarily attributed to exothermic nature of pollutant adsorption, which becomes less favorable at higher temperatures, thereby limiting the overall degradation efficiency. According to the literature, adverse effects on photocatalytic performance have been observed at temperatures approaching or exceeding 80 °C [34,35].

3.3.5. Effect of pH

Interpreting the effect of pH on the efficiency of the photodegradation process is complex due to the involvement of three reaction mechanisms. DXM degradation may proceed via hydroxyl radical ($^{\bullet}OH$) attack, direct oxidation by photogenerated h^+, or direct reduction by conducting band e^-. The contribution of each pathway depends on both the chemical nature of the pollutant and the pH of the solution. pH influences the photocatalytic process in several ways: it alters the charge distribution at the solid–liquid interface (i.e., electrical double layer), affects the surface charge of the photocatalyst relative to its P_{zc}, and modifies the sorption–desorption behavior of DXM. These changes, in turn, impact the separation and recombination dynamics of photogenerated e^-/h^+ pairs, ultimately influencing degradation efficiency [32].

In this study, the P_{zc} of the TiO_2-Zn(II)-ZC catalyst was determined to evaluate its interaction with the DXM solution. The P_{zc} is defined as the pH at which the catalyst surface has a net neutral charge. When the solution pH is lower than the P_{zc} (8.39 for TiO_2-Zn(II)-ZC), the catalyst surface is positively charged; when the pH is higher, the surface becomes negatively charged. The initial pH of the DXM solution was 5.0, and for DXM-WW, it was 7.5, both below the P_{zc}. Therefore, under these conditions, the catalyst surface remained positively charged.

DXM has two pKa values: $pKa_1 = 1.8$ and $pKa_2 = 6.18$. At pH values above its pKa, DXM exists predominantly in its ionized (negatively charged) form. Since both working pH values (5.0 and 7.5) are above pKa_1 and one is above pKa_2, DXM is partially ionized at pH 5 and fully ionized at pH 7.5. This establishes favorable electrostatic attraction between the negatively charged DXM molecules and positively charged catalyst surface, promoting adsorption and enhancing photocatalytic degradation. pH influences the dominant reactive species. At lower pH values, photogenerated h^+ plays a major role in oxidation, whereas at neutral or higher pH, $^{\bullet}OH$ are the primary oxidizing agents [32]. In both cases, pH affects the surface charge, adsorption behavior, and recombination of photogenerated e^-/h^+ pairs, thus impacting the overall photocatalytic performance [33].

3.3.6. Effect of UV Light and Accumulated Energy

UV light plays a critical role in the photodegradation of pollutants, as the degradation efficiency is strongly related to light intensity. Higher light intensities enhance the generation of reactive oxygen species and reduce the recombination rate of photogenerated e^-/h^+ pairs [18].

In this study, all Box–Behnken experiments were conducted under UV radiation, with an intensity range of 30.08–50.89 W/m^2 and accumulated energy ranging from 132.89 to 304.48 kJ/L. The highest removal efficiencies were obtained at an incident UV intensity of 41.48 W/m^2, and an accumulated energy of 134.66 kJ/L, using 5 mg/L initial DXM concentration, 30 min HRT, and M/V ratio of 1.0 mg/L. Maniakova et al. [36] studied the degradation of a pharmaceutical mixture containing carbamazepine (CBZ), diclofenac, and trimethoprim (200 µg/L each) in both deionized water and real wastewater. The Fe^{2+}/H_2O_2/ethylenediamine acid (EDDS)/sunlight process achieved 98% CBZ removal from wastewater within 60 min, with a cumulative solar energy input of 5.6 kJ/L.

3.4. Multiple Response Optimization

Statgraphics Centurion 19 software was used for multiple response optimization. This methodology was used for the identification of optimal configurations of experimental factors to simultaneously achieve the desired outcomes for multiple response variables, specifically, DXM concentration (measured by UV–Vis spectroscopy) and COD, targeted for maximization (Table 4).

Table 4. Multiple response optimization for HSP process.

Variable	Value	DXM		COD	
		Theorical	Experimental	Theorical	Experimental
Initial concentration	12.5 mg/L	74%	80.00%	62%	85.29%
HRT	60 min				
M/V	1.0 mg/L				

An optimization experiment was conducted under the following conditions: 12.5 mg/L initial DXM concentration, HRT of 60 min, and M/V ratio of 1.0 mg/L. Under these conditions, the maximum removal efficiencies achieved were 80% for DXM and 85.29% for COD, at an accumulated energy of 325.12 kJ/L. The experimental data were fitted using polynomial regression models, yielding Equations (9) and (10) for DXM degradation and COD removal, respectively.

$$\begin{aligned}\%DXM = 57.6638 + 3.01733A - 1.90825B + 59.5808C - 0.378367A^2 \\ +0.117767AB - 0.533AC + 0.0087037B^2 - 0.0333333BC - 22.1667C^2\end{aligned} \quad (9)$$

$$\begin{aligned}\%DQO = 87.7775 - 2.389A - 3.21833B + 77.845C - 0.1815A^2 \\ +0.1798AB - 1.842AC + 0.0183667B^2 - 0.178667BC - 24.27C^2\end{aligned} \quad (10)$$

In these equations, variables A, B, and C represent the initial DXM concentration (mg/L), TRH (min), and M/V ratio (mg/L), respectively.

The model adjusted for DXM degradation presented an R^2 = 0.80, considered acceptable in response surface studies [37,38], indicating that the model adequately describes experimental variability and allows its use for optimization purposes. In contrast, the COD model showed an R^2 = 0.65, reflecting a limited fit due to the comprehensive nature of this parameter, which includes both the target pollutant and oxidation byproducts, generating greater dispersion in the data. Therefore, while the DXM model can be considered predictive, COD results should be interpreted with caution and complemented with additional analyses.

3.5. Individual Effects

The individual effects were evaluated under the same conditions as those obtained in the multiple response optimization.

3.5.1. Photolysis Effect

Photolysis treatment was conducted using an initial DXM concentration of 12.5 mg/L, without the addition of catalyst, at HRT of 60 min. The UV-A radiation intensity was 45.90 W/m^2, with an accumulated energy of 193.18 KJ/L. Under these conditions, a removal efficiency of 36.8% for DXM was achieved. This partial degradation is attributed to the chemical structure of DXM, which enables absorption in the UV-A region and part of the visible spectrum. Such absorption promotes the photolysis of specific bonds, particularly C−O and C−H, leading to partial molecular breakdown under solar irradiation [8].

3.5.2. Effect of Catalyst (TiO_2-Zn(II)-ZC) Without Solar Radiation

The experiment was performed using an initial DXM concentration of 12.5 mg/L, HRT of 60 min, and a catalyst M/V ratio of 1mg/L TiO_2-Zn(II)-ZC, in the absence of solar radiation. Under these conditions, the DXM removal efficiency was only 3.2%. This result confirms that the TiO_2-Zn(II)-ZC photocatalyst requires UV irradiation to activate the generation of e^-/h^+ pairs and the subsequent formation of reactive oxidative species such as $^{\bullet}OH$ and $O_2^{\bullet-}$ radicals, which are essential for the degradation of organic compounds [17].

3.5.3. Effect of Catalyst TiO_2-Zn(II)-ZC Under UV Radiation Lamp

The treatment was conducted at a DXM concentration of 12.5 mg/L, with HRT of 60 min, a catalyst M/V ratio of 1 mg/L TiO_2-Zn(II)-ZC, and exposure to a GS-T5.003 lamp (5 W, λ = 380–400 nm and 16 W/m^2). Under these conditions, the DXM removal efficiency was low, achieving only 8%. Photocatalytic activity occurs when the energy of incident photon is equal to or greater than the bandgap energy of the photocatalyst, enabling the generation of e^-/h^+ pairs [39]. According to Liu et al. [40] TiO_2-Zn doped materials exhibit photocatalytic activity at λ > 429 nm. Therefore, the low efficiency observed in this experiment is associated with insufficient power and spectral output of the UV lamp, which did not provide adequate energy to initiate photocatalytic reactions. Asgari et al. [41] achieved 87% DXM removal using a UV/H_2O_2/MgO system under optimized conditions: 20 mg/L DXM, 0.5 mM H_2O_2, 30 min of HRT, pH = 3, and 55W UV radiation. Figure 8 presents a comparative overview of the individual effects and optimization of the HSP process on DXM degradation.

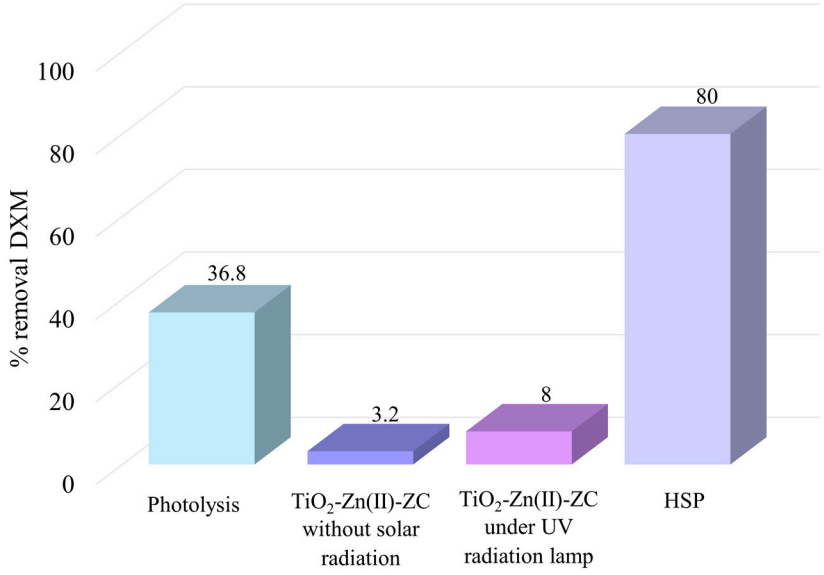


Figure 8. Comparison of the individual effects on DXM degradation.

3.6. Kinetic Parameters

The kinetics of DXM degradation were evaluated in 12.5 mg/L DXM-WW under the optimal conditions established through multiple response optimization: 12.5 mg/L DXM, HRT of 60 min, and a catalyst M/V ratio of 1.0 mg/L TiO_2-Zn(II)-ZC. Along with COD and DXM measurements by UV–Vis, HPLC analysis was performed to monitor degradation. Figure 9 shows the kinetics of degradation of the aqueous DXM solution (Figure 9a) and DXM-WW (Figure 9b), showing the relationship between DXM concentration vs. and accumulated energy in the system. The maximum DXM removal achieved was 88.71% for the aqueous solution and 67.88% for DXM-WW. In both cases, equilibrium was achieved at approximately 100 kJ/L of accumulated energy.

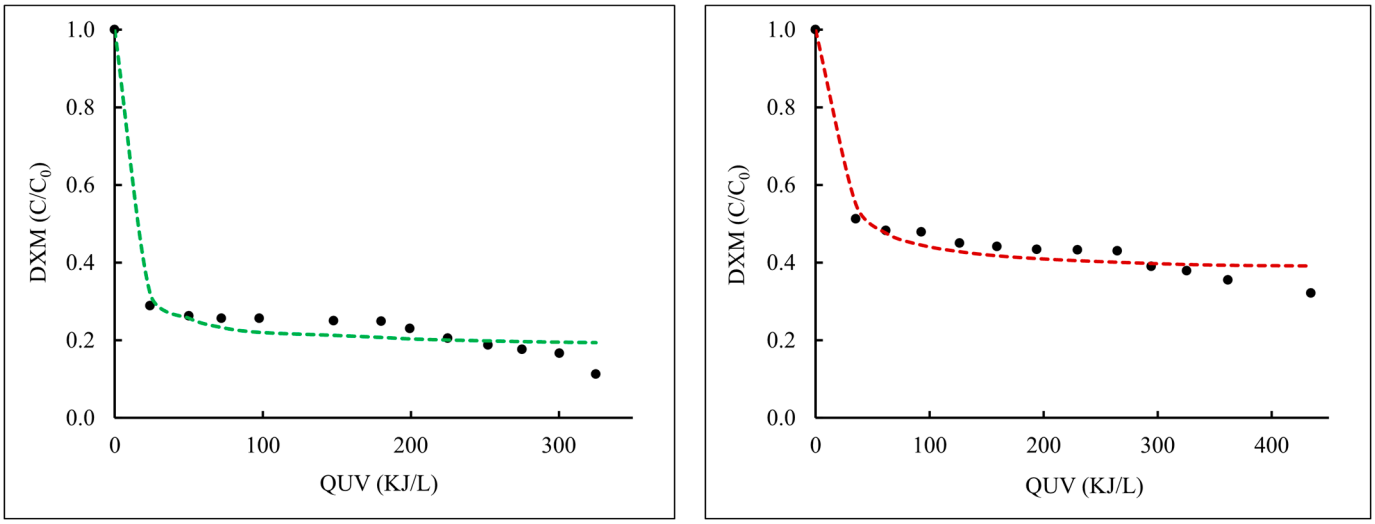


Figure 9. Degradation kinetics of (**a**) DXM in aqueous solution, and (**b**) DXM-WW fitted to the BMG model: DXM (C/C_0) Vs. QUV (kJ/L). • Data, --- BMG model, --- BMG model.

Table 5 shows the kinetic constants and coefficients of determination (R^2) for the first-order, second-order, and BMG models applied to both the aqueous DXM solution and DXM-WW. Among these, the BMG model showed the best fit, as reflected by the R^2 values for the aqueous solution: DXM = 0.9021, COD = 0.9837, and HPLC = 0.9875. For the DXM-WW system, the BMG model also exhibited a stronger fit for UV–Vis and HPLC results (DXM = 0.9671 and HPLC = 0.9811), whereas COD was described by the first-order model (R^2 = 0.9728). The results are summarized in Table 5.

Table 5. Kinetic constants of DXM removal in aqueous solution and DXM-WW.

Aqueous Solution	**First Order**		**Second Order**		**BMG**		
Quantification Technique	**K (m^{-1})**	**R^2**	**K (L/mg min)**	**R^2**	**m (min)**	**b**	**R^2**
UV–Vis	0.0213	0.8859	0.0026	0.9020	30.9402	0.9768	0.9021
COD	0.0116	0.8416	0.0002	0.8025	279.901	−3.4414	0.9837
HPLC	0.0848	0.6190	0.0151	0.8987	1.2717	1.2197	0.9875
DXM-WW	First order		Second order		BMG		
Quantification technique	K (m^{-1})	R^2	K (L/mg min)	R^2	m (min)	b	R^2
UV–Vis	0.0366	0.9512	0.0055	0.9627	18.0761	0.8829	0.9671
COD	0.0676	0.9728	0.0016	0.9330	11.559	0.8067	0.9619
HPLC	0.0273	0.1493	0.0040	0.7043	3.1790	1.5895	0.9811

The BMG model characterizes the two-stage kinetics typical of AOPs. In this model, the parameter m represents the degradation rate governed by •OH generation, and b corresponds to the maximum achievable DXM removal. Typically, higher values of m and b indicate a slower degradation, whereas lower values reflect faster kinetics and more efficient degradation [42].

Grilla et al. [12] investigated DXM degradation through simultaneous electrochemical oxidation and simulated solar irradiation, using a boron-doped diamond anode and a stainless-steel cathode in a 0.1 M $NaSO_4$ electrolyte. Under conditions of 0.5 mg/L DXM, 0.2 A/m^2 current density, 150 mg/L persulfate, 60 min HRT, and natural solution pH, they achieved 95% DXM removal with a pseudo-first-order rate constant of K = 0.194 min^{-1}. Shookohi et al. [13] evaluated DXM removal using an UV/$S_2O_8{}^{2-}$/Al_2O_3 process. At 20 mg/L DXM, pH = 3, 0.5 nM persulfate, 30 min HRT, and 55 W UV lamp, they reported a rate constant of K= 0.0878 min^{-1}.

3.7. DXM-Wastewater Treatment

To evaluate the effectiveness of the HSP process in treating DXM-WW, a comprehensive physicochemical characterization was performed. The experiments were conducted under optimized conditions: 12.5 mg/L DXM, HRT of 60 min, and a catalyst M/V ratio of 1.0 mg/L. Table 6 presents the results for both DXM aqueous solution and DXM-WW, before and after HSP treatment.

Table 6. Physicochemical characterization of DXM aqueous solution.

Parameter	Units	Aqueous Solution			DXM-WW		
		Initial	Final	% Removal	Initial	Final	% Removal
DXM-UV	mg/L	12.5	2.5	80	12.5	1.2	90.4
DXM-HPLC	mg/L	12.5	1.41	88.71	12.5	4.01	67.88
COD	mg/L	68	10	85.29	86	6	93.02
TOC	mg/L	35	6	82.86	63	4.8	92.38
pH	U pH	5	6.5	-	7.5	7.5	-
Color	Pt-Co	0	0	-	355	56	84.22
Turbidity	NTU	0	5	-	147	45	69.38
BOD_5	mg/L	5.56	2.67	48.02	18	4	77.77
BOD_5/COD		0.081	0.267	-	0.209	0.666	-
Nitrates	mg/L $NO_3{}^{-}$-N	1.339	0	100	2.203	1.471	33.22
Nitrites	mg/L $NO_2{}^{-}$-N	0.039	0	100	0.263	0.109	58.55
Phosphate	mg/L $PO_4{}^{3-}$	2.456	2.280	7.16	5.893	3.817	35.22
Total phosphorus	mg/L $PO_4{}^{3-}$-P	0.802	0.792	11.59	6.520	8.456	-
Chlorides	mg/L Cl^{-}	9.7	5.4	55.67	76.3	65.5	14.15
Sulfates	mg/L $SO_4{}^{2-}$	3.4	0	100	24.8	13.5	45.56

For the DXM aqueous solution, the HSP system demonstrated high removal efficiencies for organic contaminants: with 80% DXM removal by UV–Vis and 88.71% by HPLC, as well as COD removal of 85.29%, and COT removal of 82.86%. BOD_5 decreased from 5.56 to 2.67 mg/L, and the biodegradability index increased from 0.081 to 0.267. In terms of inorganic parameters, the process exhibited excellent removal efficiencies, with nitrates, nitrites, and sulfates being removed by 100%. Chlorides were removed by 55.67%, and total phosphorus and phosphates by 11.59% and 7.16%, respectively. Additionally, the pH increased from 5.0 to 6.5 after treatment, which may contribute to the improved removal of weak acids and bases such as nitrates, sulfates, and chlorides.

For the DXM-WW, the HSP process demonstrated notable treatment efficiency under optimized conditions; 90.40% DXM removal by UV–Vis, 67.88% DXM by HPLC, 93.02%

COD, and 92.38% TOC were achieved. BOD_5 decreased significantly from 18 mg/L to 4 mg/L (a 77.77% reduction), and the biodegradability index improved from 0.209 to 0.667. Color and turbidity removal was 84.22% and 69.38%, respectively. Regarding inorganic compounds, the following removal efficiencies were observed; nitrates 33.22%, nitrites 58.55%, chlorides 14.15%, sulfates 45.56%, and phosphates 35.22%. Total phosphorus increased from 6.520 mg/L to 8.456 mg/L after treatment. The pH of DXM-WW remained stable at 7.5 after treatment.

According to the results in aqueous solution, the HSP process promotes DXM degradation (88.71% HPLC). Meanwhile, in DXM-WW, the removal was decreased to 67.88%, due to the matrix complexity. The removal of COD and TOC were higher in DXM-WW than aqueous solution, because these organic parameters quantify the biodegradable organic matter and persistent (DXM).

3.8. Mechanism

The activation of TiO_2 is dependent on the wavelength of the incident radiation and the bandgap of the material, the energy difference between the VB and CB. Photocatalytic activation occurs when the energy of the incoming photon (hν) is equal to or greater than the bandgap energy (Equation (11)), enabling the generation of e^-/h^+ pairs. Once excited, the positive h^+ in the VB can oxidize surface-bound water molecules or HO^- radicals, which are highly reactive oxidizing agents in photocatalytic processes (Equations (12) and (13)). Meanwhile, photogenerated e^- in the CB can reduce dissolved oxygen, forming superoxide anion radicals (Equation (14)). These reactive oxygen species, including $^{\bullet}OH$, $HO^{\bullet}{}_2$, $O_2{}^{\bullet-}$ and H_2O_2, can also form through subsequent chain reactions, outlined in Equations (14)–(20), sustaining the radical based degradation cycle as long as light energy is available. The $^{\bullet}OH$ radical is considered the primary oxidizing species for the photocatalytic degradation of organic pollutants. However, the efficiency of the photocatalytic process can be significantly reduced by the recombination of e^-/h^+ pairs, which dissipates energy as heat rather than enabling redox reactions. Therefore, suppressing e^-_{CB}/h^+_{VB} recombination is essential for enhancing photocatalytic performance.

$$TiO_2 - Zn(II) - ZC + h\nu \rightarrow TiO_2 - Zn(II) - ZC^*\left(e^-_{CB} + h^+_{VB}\right) \quad (11)$$

$$TiO_2 - Zn(II) - ZC^*\left(h^+_{VB}\right) + H_2O \rightarrow TiO_2 - Zn(II) - ZC^*\left(h^+_{VB}\right) + H^+ + HO^{\bullet} \quad (12)$$

$$TiO_2 - Zn(II) - ZC^*\left(h^+_{VB}\right) + OH^- \rightarrow TiO_2 - Zn(II) - ZC^*\left(h^+_{VB}\right) + HO^{\bullet} \quad (13)$$

$$TiO_2 - Zn(II) - ZC^*\left(e^-_{cB}\right) + O_2 \rightarrow TiO_2 - Zn(II) - ZC^*\left(e^-_{cB}\right) + O_2^{\bullet-} \quad (14)$$

$$TiO_2 - Zn(II) - ZC^*\left(h^+_{VB}\right) + 2H_2O \rightarrow TiO_2 - Zn(II) - ZC^*\left(h^+_{VB}\right) + 2H^+ + H_2O_2 \quad (15)$$

$$TiO_2 - Zn(II) - ZC^*\left(e^-_{cB}\right) + O_2^{\bullet-} + 2H^+ \rightarrow TiO_2 - Zn(II) - ZC^*\left(e^-_{cB}\right) + H_2O_2 \quad (16)$$

$$O_2^{\bullet-} + 2H^+ \rightarrow H_2O_2 \quad (17)$$

$$H_2O_2 + e^-_{cB} \rightarrow HO^{\bullet} + HO^- \quad (18)$$

$$O_2^{\bullet-} + H^+ \rightarrow HO_2^{\bullet} \quad (19)$$

$$HO_2^{\bullet} + HO_2^{\bullet} \rightarrow H_2O_2 + O_2 \quad (20)$$

An electron in the CB can participate in the reduction of DXM while a hole in the VB can facilitate its oxidization [39]. However, in heterogeneous photocatalysis, oxidative pathways are generally more dominant and efficient than reductive pathways (Figure 10).

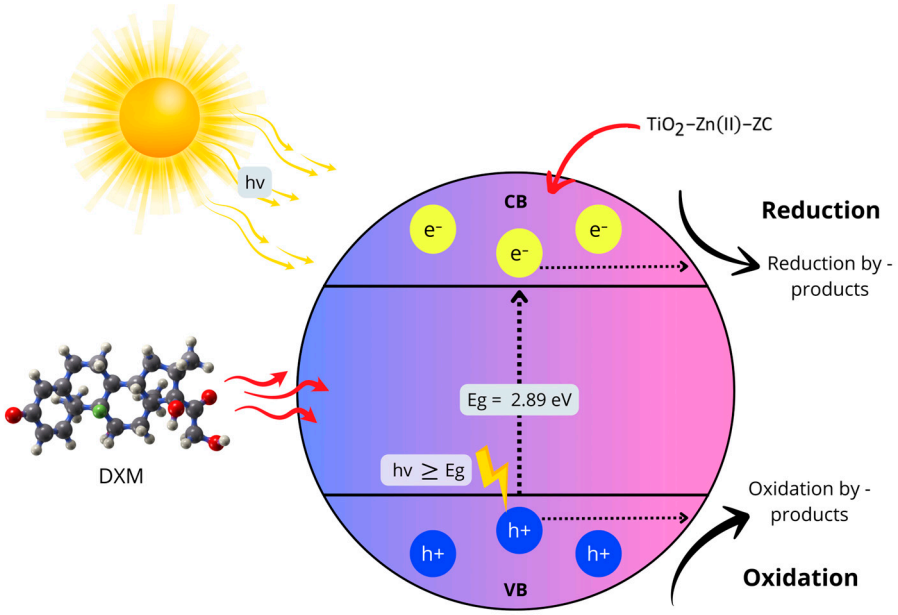


Figure 10. Mechanism degradation DXM by HSP.

Based on previous reports [43], as well as IR and fluorescence spectroscopy analysis before and after HSP treatment (Figures S2 and S3, Supplementary Materials), a mechanism for DXM degradation was proposed. The degradation follows a non-selective oxidation pathway predominantly driven by interactions with •OH. Due to its high electronegativity, F attracts electrons and can form bonds with Zn species supported on the zeolite surface, facilitating adsorption and reaction acceleration. In the initial phase of HSP process, hydrolysis leads to the cleavage of F and phosphate groups from the DXM molecule ($C_{22}H_{31}FO_8P$) [29]. Subsequently, •OH radicals targets the electron-rich methylene groups and double bonds within the molecular rings of DXM, initiating oxidative ring-opening reactions. This results in the formation of lower molecular weight intermediates such as $C_{11}H_{14}O_5$ and ($C_{10}H_{18}O_4$). Further decarboxylation and oxidation steps yield compounds including $C_9H_{16}O_4$, $C_8H_{16}O_2$, $C_6H_{14}O_2$, and $C_4H_8O_3$. The ultimate degradation products are acetic acid ($C_2H_4O_2$), formaldehyde (CH_2O), and carbon dioxide (CO_2) [41], indicating a progressive reduction in molecular weight of the by-products during the photocatalytic reaction [44].

4. Conclusions

In this study, the synthesis of a modified TiO_2-Zn-clinoptilolite catalyst via the electrodeposition method and its application in HSP for the degradation of aqueous DXM and DXM-WW were evaluated.

The synthesis and application of TiO_2-Zn(II)-ZC by the electrodeposition method successfully reduced the bandgap of TiO_2, enabling the utilization of solar irradiation for the generation of e^-/h^+ pairs and reactive oxidative species such as •OH, H_2O_2, and $O_2^{\bullet-}$, which facilitated the effective photodegradation of DXM and improved wastewater quality.

Multiple response optimization identified the optimal conditions in aqueous solution: 12.5 mg/L DXM, HRT of 60 min, and M/V ratio 1.0 mg/L, achieving maximum removal efficiencies: 88.71% DXM (HPLC), 85.29% COD, and 82.86% TOC, under conditions of 67 °C, 325.12 kJ/L accumulated energy, and 38.77 W/m^2 incident radiation.

For DXM-WW enriched with 12.5 mg/L DXM, removal efficiencies reached 67.88% DXM (HPLC), 93.02% COD, and 92.38% TOC, with the biodegradability index increasing from 0.209 to 0.667, at 69.4 °C, 434.51 kJ/L, and incident radiation of 50.47 W/m^2.

These results demonstrate that the catalyst synthetized TiO_2-Zn(II)-ZC by electrodeposition was highly efficient in the removal DXM in aqueous solution and wastewater.

Supplementary Materials: The following supporting information can be downloaded at: https://www.mdpi.com/article/10.3390/pr13092781/s1, Figure S1: EDS spectra: (a) ZC, (b) TiO_2-Zn(II)-ZC (initial). After HSP: (c) TiO_2-Zn(II)-ZC (M/V 0.5), (d) TiO_2-Zn(II)-ZC (M/V 1.0), (e) TiO_2-Zn(II)-ZC (M/V 1.5); Figure S2: IR spectra after HSP treatment of (a) DXM in aqueous solution and (b) DXM-WW; Figure S3: Fluorescence spectroscopy of samples: (a) and (b) DXM solution before and after HSP treatment respectively, (c) and (d) DXM-WW before and after HSP treatment, respectively. Table S1: Experimental Matrix; Table S2: IR bands and corresponding functional groups associated with ZC, TiO_2 and TiO_2-Zn(II)-ZC; Table S3: Characteristic IR bands associated with DXM in aqueous solution; Table S4. Analysis of variance (ANOVA) showing the statistical significance of factors influencing the HSP process.

Author Contributions: Conceptualization, I.L.-H. and M.C.-J.; methodology, A.G.B.-P.; software, E.A.T.-S. and M.E.-S.; validation, F.S.-T. and M.S.-R.; formal analysis, V.M.-M.; investigation, resources, and data curation, A.G.B.-P., M.C.-J. and I.L.-H.; writing—original draft preparation, A.G.B.-P., M.C.-J. and I.L.-H.; writing—review and editing, V.M.-M. and C.R.F.; visualization, supervision, project administration, and funding acquisition I.L.-H. and V.M.-M. All authors have read and agreed to the published version of the manuscript.

Funding: This research was funded by Universidad Autónoma del Estado de México, funding number 7214/2025CIB.

Data Availability Statement: The original contributions presented in this study are included in the article. Further inquiries can be directed to the corresponding author.

Acknowledgments: This work was supported by Universidad Autónoma del Estado de México (project 7214/2025CIB) and the scholarship for Briseño-Peña (1289857) awarded by the Secretaria de Ciencia, Humanidades, Tecnología e Innovación (SECIHTI), México.

Conflicts of Interest: The authors declare no conflicts of interest.

Abbreviations

The following abbreviations are used in this manuscript:

DXM	Dexamethasone
HSP	Heterogeneous solar photocatalysis
DXM-WW	Chocolate industry wastewater
ZC	Zeolite clinoptilolite
HRT	Hydraulic retention time
M/V	Catalyst mass/solution volume
VB	Valence band
CB	Conduction band

References

1. Schröder, S.; Ortiz, I.; San-Román, M.-F. Electrochemical Degradation of Key Drugs to Treat COVID-19: Experimental Analysis of the Toxic by-Products Formation (PCDD/Fs). *Sci. Total Environ.* **2024**, *906*, 167660. [CrossRef] [PubMed]
2. Arvaniti, O.S.; Ioannidi, A.; Politi, A.; Miserli, K.; Konstantinou, I.; Mantzavinos, D.; Frontistis, Z. Dexamethasone Degradation in Aqueous Medium by a Thermally Activated Persulfate System: Kinetics and Transformation Products. *J. Water Process Eng.* **2022**, *49*, 103134. [CrossRef]
3. Onga, L.; Kattel-Salusoo, E.; Preis, S.; Dulova, N. Degradation of Anti-Inflammatory Drug Dexamethasone by Pulsed Corona Discharge: The Effect of Peroxycompounds Addition. *J. Environ. Chem. Eng.* **2022**, *10*, 108042. [CrossRef]
4. Salari, M.; Akbari, H.; Adibzadeh, A.; Akbari, H. Modeling and Optimization of Advanced Oxidation Treatment of Dexamethasone from Aquatic Solutions Using Electro-Peroxone/Ultrasonic Process: Application for Real Wastewater, Electrical Energy Consumption and Degradation Pathway. *Sep. Purif. Technol.* **2023**, *327*, 124871. [CrossRef]

5. Ghenaatgar, A.; M.A.Tehrani, R.; Khadir, A. Photocatalytic Degradation and Mineralization of Dexamethasone Using WO3 and ZrO2 Nanoparticles: Optimization of Operational Parameters and Kinetic Studies. *J. Water Process Eng.* **2019**, *32*, 100969. [CrossRef]
6. Salari, M.; Alahabadi, A.; Rahmani-Sani, A.; Miri, M.; Yazdani-Aval, M.; Lotfi, H.; Saghi, M.H.; Rastegar, A.; Sepehr, M.N.; Darvishmotevalli, M. A Comparative Study of Response Surface Methodology and Artificial Neural Network Based Algorithm Genetic for Modeling and Optimization of EP/US/GAC Oxidation Process in Dexamethasone Degradation: Application for Real Wastewater, Electrical Energy Consumption. *Chemosphere* **2024**, *349*, 140832. [CrossRef]
7. Ioannidi, A.A.; Arvaniti, O.S.; Miserli, K.; Konstantinou, I.; Frontistis, Z.; Mantzavinos, D. Removal of Drug Dexamethasone from Aqueous Matrices Using Low Frequency Ultrasound: Kinetics, Transformation Products, and Effect of Microplastics. *J. Environ. Manag.* **2023**, *328*, 117007. [CrossRef]
8. Quaresma, A.V.; Rubio, K.T.S.; Taylor, J.G.; Sousa, B.A.; Silva, S.Q.; Werle, A.A.; Afonso, R.J.C.F. Removal of Dexamethasone by Oxidative Processes: Structural Characterization of Degradation Products and Estimation of the Toxicity. *J. Environ. Chem. Eng.* **2021**, *9*, 106884. [CrossRef]
9. Rodríguez-Peña, M.; Natividad, R.; Barrera-Díaz, C.E.; Balderas Hernández, P.; Alanis Ramírez, C.I.; Roa-Morales, G. Current Perspective of Advanced Electrochemical Oxidation Processes in Wastewater Treatment and Life Cycle Analysis. *Int. J. Electrochem. Sci.* **2024**, *19*, 100589. [CrossRef]
10. Preethi, S.P.S.; Kumar, G.; Yogalakshmi, K.N.; Gunasekaran, M.; Banu, J.R. Recent Progress in Mineralization of Emerging Contaminants by Advanced Oxidation Process: A Review. *Environ. Pollut.* **2024**, *341*, 122842. [CrossRef]
11. Arman, K.; Baghdadi, M.; Pardakhti, A. Photochemical Degradation of Dexamethasone by UV/Persulphate, UV/Hydrogen Peroxide and UV/Free Chlorine Processes in Aqueous Solution Using Response Surface Methodology (RSM). *Int. J. Environ. Anal. Chem.* **2024**, *104*, 2056–2074. [CrossRef]
12. Grilla, E.; Taheri, M.E.; Miserli, K.; Venieri, D.; Konstantinou, I.; Mantzavinos, D. Degradation of Dexamethasone in Water Using BDD Anodic Oxidation and Persulfate: Reaction Kinetics and Pathways. *J. Chem. Technol. Biotechnol.* **2021**, *96*, 2451–2460. [CrossRef]
13. Shookohi, R.; Faraji, H.; Arabkohsar, A.; Salari, M.; Mahmoudi, M.M. The Efficiency of UV/S2O82− Photo-Oxidation Process in the Presence of Al2O3 for the Removal of Dexamethasone from Aqueous Solution: Kinetic Studies. *Water Sci. Technol.* **2019**, *79*, 938–946. [CrossRef] [PubMed]
14. Sarkhosh, M.; Azizi, S.; Mokrani, T.; Seopela, M.; Maaza, M. Simultaneous Cr(VI) Reduction and Dexamethasone Phosphate Oxidation with Organo-Metallic Sludge Formation Under UV Irradiation: Kinetics, Degradation Pathways, and Mechanism. *Arab. J. Sci. Eng.* **2024**, *49*, 9413–9424. [CrossRef]
15. Balapure, A.; Ray Dutta, J.; Ganesan, R. Recent Advances in Semiconductor Heterojunctions: A Detailed Review of the Fundamentals of Photocatalysis, Charge Transfer Mechanism and Materials. *RSC Appl. Interfaces* **2024**, *1*, 43–69. [CrossRef]
16. do Nascimento, R.C.; Cahino, A.; Lucena, L.G.; Barbosa Segundo, I.D.; Espíndola, J.C.; Rocha, E.M.R. A Systematic Review of Heterogeneous Catalysis Applied to the Treatment of Pharmaceutical Wastewater: Operational Conditions and Statistical Analysis. *Photochem.* **2024**, *4*, 285–301. [CrossRef]
17. Chen, X.; Rong, H.; Ndagijimana, P.; Nkinahamira, F.; Kumar, A.; Guo, D.; Cui, B. Towards Removal of PPCPs by Advanced Oxidation Processes: A Review. *Results Eng.* **2023**, *20*, 101496. [CrossRef]
18. Lee, D.E.; Kim, M.K.; Danish, M.; Jo, W.K. State-of-the-Art Review on Photocatalysis for Efficient Wastewater Treatment: Attractive Approach in Photocatalyst Design and Parameters Affecting the Photocatalytic Degradation. *Catal. Commun.* **2023**, *183*, 106764. [CrossRef]
19. Castañeda-Juárez, M.; Linares-Hernández, I.; Martínez-Miranda, V.; Teutli-Sequeira, E.A.; Castillo-Suárez, L.A.; Sierra-Sánchez, A.G. SARS-CoV-2 Pharmaceutical Drugs: A Critical Review on the Environmental Impacts, Chemical Characteristics, and Behavior of Advanced Oxidation Processes in Water. *Environ. Sci. Pollut. Res.* **2022**, *29*, 67604–67640. [CrossRef]
20. Hu, G.; Yang, J.; Duan, X.; Farnood, R.; Yang, C.; Yang, J.; Liu, W.; Liu, Q. Recent Developments and Challenges in Zeolite-Based Composite Photocatalysts for Environmental Applications. *Chem. Eng. J.* **2021**, *417*, 129209. [CrossRef]
21. Slavova, M.; Slavov, I.; Terziev, V.; Mladenova, E.; Abrashev, B. Application of Zeolite and Comparable Porous Materials for Enhancing the Performance of Different Types of Secondary Batteries: A Review Article. *J. Energy Storage* **2024**, *98*, 112949. [CrossRef]
22. Castañeda-Juárez, M.; Martínez-Miranda, V.; Almazán-Sánchez, P.T.; Linares-Hernández, I.; Santoyo-Tepole, F.; Vázquez-Mejía, G. Synthesis of TiO 2 Catalysts Doped with Cu, Fe, and Fe/Cu Supported on Clinoptilolite Zeolite by an Electrochemical-Thermal Method for the Degradation of Diclofenac by Heterogeneous Photocatalysis. *J. Photochem. Photobiol. A Chem.* **2019**, *380*, 111834. [CrossRef]
23. Belalcázar-Saldarriaga, A.; Prato-Garcia, D.; Vasquez-Medrano, R. Photo-Fenton Processes in Raceway Reactors: Technical, Economic, and Environmental Implications during Treatment of Colored Wastewaters. *J. Clean. Prod.* **2018**, *182*, 818–829. [CrossRef]

24. Peschke, S.F. Synthesis and Characterization of Rare-Earth Oxide Transition-Metal Arsenides and Selenides. Ph.D. Thesis, Universität München, Munich, Germany, 2017.
25. De Luca, A.; De Benedetto, A.; De Matteis, V.; Cascione, M.; Di Corato, R.; Ingrosso, C.; Corrado, M.; Rinaldi, R. Eco-Friendly TiO2 Nanoparticles: Harnessing Aloe Vera for Superior Photocatalytic Degradation of Methylene Blue. *Catalysts* **2024**, *14*, 820. [CrossRef]
26. Muñoz-Aguirre, N.; Martínez-Pérez, L.; Muñoz-Aguirre, S.; Flores-Herrera, L.A.; Vergara Hernández, E.; Zelaya-Angel, O. Luminescent Properties of (004) Highly Oriented Cubic Zinc Blende ZnO Thin Films. *Materials* **2019**, *12*, 3314. [CrossRef]
27. Long, J.; Nand, A.V.; Bunt, C.; Seyfoddin, A. Controlled Release of Dexamethasone from Poly(Vinyl Alcohol) Hydrogel. *Pharm. Dev. Technol.* **2019**, *24*, 839–848. [CrossRef]
28. Abdu, M.; Tibebu, S.; Babaee, S.; Worku, A.; Msagati, T.A.M.; Nure, J.F. Optimization of Photocatalytic Degradation of Eriochrome Black T from Aqueous Solution Using TiO2-Biochar Composite. *Results Eng.* **2025**, *25*, 104036. [CrossRef]
29. Pazoki, M.; Parsa, M.; Farhadpour, R. Removal of the Hormones Dexamethasone (DXM) by Ag Doped on TiO2 Photocatalysis. *J. Environ. Chem. Eng.* **2016**, *4*, 4426–4434. [CrossRef]
30. Wilk, J.; Sowik, P.; Stando, K.; Grabowska, A.; Felis, E.; Bajkacz, S. Effect of Sunlight-Initiated Processes on Dexamethasone Degradation in Liquid Samples. *Desalination Water Treat.* **2025**, *321*, 101042. [CrossRef]
31. Wang, T.; Zhou, Z.; Liu, C.; Li, X.; Zhao, Y. Stability of a Novel Integrated Photocatalysis-Ultrafiltration Reactor: Algal Organic Matter Removal and Membrane Fouling Alleviation Mechanism. *J. Memb. Sci.* **2025**, *717*, 123602. [CrossRef]
32. Akpan, U.G.; Hameed, B.H. Parameters Affecting the Photocatalytic Degradation of Dyes Using TiO_2-Based Photocatalysts: A Review. *J. Hazard. Mater.* **2009**, *170*, 520–529. [CrossRef]
33. Mishra, S.; Sundaram, B. A Review of the Photocatalysis Process Used for Wastewater Treatment. *Mater. Today Proc.* **2023**, *102*, 393–409. [CrossRef]
34. Chakravorty, A.; Roy, S. A Review of Photocatalysis, Basic Principles, Processes, and Materials. *Sustain. Chem. Environ.* **2024**, *8*, 100155. [CrossRef]
35. Chen, Y.-W.; Hsu, Y.-H. Effects of Reaction Temperature on the Photocatalytic Activity of TiO_2 with Pd and Cu Cocatalysts. *Catalysts* **2021**, *11*, 966. [CrossRef]
36. Maniakova, G.; Kowalska, K.; Murgolo, S.; Mascolo, G.; Libralato, G.; Lofrano, G.; Sacco, O.; Guida, M.; Rizzo, L. Comparison between Heterogeneous and Homogeneous Solar Driven Advanced Oxidation Processes for Urban Wastewater Treatment: Pharmaceuticals Removal and Toxicity. *Sep. Purif. Technol.* **2020**, *236*, 116249. [CrossRef]
37. Myers, R.H.; Montgomery, D.C.; Anderson-Cook, C. Response Surface Methodology: Process and Product Optimization Using Designed Experiments. *Response Surf. Methodol.* **2016**, *705*, 328–335.
38. Montgomery, D. *Design and Analysis of Experiments*, 9th ed.; John Wiley & Sons, Inc.: Sedona, AZ, USA, 2017; Volume 1.
39. Hassaan, M.A.; El-Nemr, M.A.; Elkatory, M.R.; Ragab, S.; Niculescu, V.-C.; El Nemr, A. Principles of Photocatalysts and Their Different Applications: A Review. *Top. Curr. Chem.* **2023**, *381*, 31. [CrossRef]
40. Liu, X.H.; Deng, Y.; Zhang, Y.C.; Zhou, Y.H. Characterization on the Microstructures and Optical Performances of TiO_2 Doped with Transition Metals. In Proceedings of the International Conference on Advanced Materials (ICAM 2013), Qingdao, China, 23–27 September 2013; Volumes 887–888, pp. 388–394.
41. Asgari, G.; Salari, M.; Molla Mahmoudi, M.; Jamshidi, R.; Dehdar, A.; Faraji, H.; Zabihollahi, S.; Alizadeh, S. Kinetic Studies of Dexamethasone Degradation in Aqueous Solution via a Photocatalytic UV/$H2O_2$/MgO Process. *Sci. Rep.* **2022**, *12*, 21360. [CrossRef]
42. Kumar, J.E.; Mulai, T.; Tripathy, A. Behnajady-Modirshahla-Ghanbary Kinetic Model for Degradation of Azo Dye Using Fenton Oxidation Process: A Mini Review. *Next Res.* **2024**, *1*, 100047. [CrossRef]
43. Guo, Z.; Guo, A.; Guo, Q.; Rui, M.; Zhao, Y.; Zhang, H.; Zhu, S. Decomposition of Dexamethasone by Gamma Irradiation: Kinetics, Degradation Mechanisms and Impact on Algae Growth. *Chem. Eng. J.* **2017**, *307*, 722–728. [CrossRef]
44. Ziembowicz, S.; Kida, M. Limitations and Future Directions of Application of the Fenton-like Process in Micropollutants Degradation in Water and Wastewater Treatment: A Critical Review. *Chemosphere* **2022**, *296*, 134041. [CrossRef] [PubMed]

Disclaimer/Publisher's Note: The statements, opinions and data contained in all publications are solely those of the individual author(s) and contributor(s) and not of MDPI and/or the editor(s). MDPI and/or the editor(s) disclaim responsibility for any injury to people or property resulting from any ideas, methods, instructions or products referred to in the content.